Photo-induced second-order nonlinearity in stoichiometric silicon nitride waveguides

Marco A.G. Porcel,[1] Jesse Mak,[1] Caterina Taballione,[1] Victoria K. Schermerhorn,[1] Jörn P. Epping,[1,2] Peter J.M. van der Slot,[1,*] and Klaus-J. Boller[1]

[1]*Laser Physics and Nonlinear Optics, Mesa$^+$ Institute for Nanotechnology, Department of Science and Technology, University of Twente, Enschede, The Netherlands*
[2]*Currently with LioniX International BV. Enschede, The Netherlands*
*p.j.m.vanderslot@utwente.nl

Abstract: We report the observation of second-harmonic generation (SHG) in stoichiometric silicon nitride waveguides grown via low-pressure chemical vapor deposition (LPCVD). Quasi-rectangular waveguides with a large cross section were used, with a height of 1 μm and various different widths, from 0.6 to 1.2 μm, and with various lengths from 22 to 74 mm. Using a mode-locked laser delivering 6-ps pulses at 1064 nm wavelength with a repetition rate of 20 MHz, 15% of the incoming power was coupled through the waveguide, making maximum average powers of up to 15 mW available in the waveguide depending on the waveguide cross section. Second-harmonic output was observed with a delay of minutes to several hours after the initial turn-on of pump radiation, showing a fast growth rate between 10^{-4} to 10^{-2} s^{-1}, with the shortest delay and highest growth rate at the highest input power. After this first, initial build-up (observed delay and growth), the second-harmonic became generated instantly with each new turn-on of the pump laser power. Phase matching was found to be present independent of the used waveguide width, although the latter changes the fundamental and second-harmonic phase velocities. We address the presence of a second-order nonlinearity and phase matching, involving an initial, power-dependent build-up, to the coherent photogalvanic effect. The effect, via the third-order nonlinearity and multiphoton absorption leads to a spatially patterned charge separation, which generates a spatially periodic, semi-permanent, DC-field-induced second-order susceptibility with a period that is appropriate for quasi-phase matching. The maximum measured second-harmonic conversion efficiency amounts to 0.4% in a waveguide with 0.9×1 μm^2 cross section and 36 mm length, corresponding to 53 μW at 532 nm with 13 mW of IR input coupled into the waveguide. The maximum equivalent $\chi^{(2)}$-susceptibility amounts to 3.7 pm/V, as retrieved from the measured conversion efficiency.

References and links

1. L. Pavesi, *Silicon Photonics* (Springer, 2004).
2. T. Tekin, N. Pleros, R. Pitwon, and A. Hakansson, *Optical Interconnects for Data Centers* (Woodhead Publishing, 2016).
3. R. Hunsperger, *Integrated Optics: Theory and Technology* (Springer, 2013).
4. M. Smit, X. Leijtens, H. Ambrosius, E. Bente, J. van der Tol, B. Smalbrugge, T. de Vries, E.-J. Geluk, J. Bolk, R. van Veldhoven, L. Augustin, P. Thijs, D. D'Agostino, H. Rabbani, K. Lawniczuk, S. Stopinski, S. Tahvili, A. Corradi, E. Kleijn, D. Dzibrou, M. Felicetti, E. Bitincka, V. Moskalenko, J. Zhao, R. Santos, G. Gilardi, W. Yao, K. Williams, P. Stabile, P. Kuindersma, J. Pello, S. Bhat, Y. Jiao, D. Heiss, G. Roelkens, M. Wale, P. Firth, F. Soares, N. Grote, M. Schell, H. Debregeas, M. Achouche, J.-L. Gentner, A. Bakker, T. Korthorst, D. Gallagher, A. Dabbs, A. Melloni, F. Morichetti, D. Melati, A. Wonfor, R. Penty, R. Broeke, B. Musk, and D. Robbins, "An introduction to InP-based generic integration technology," Semicond. Sci. Technol. **29**, 083001 (2014).
5. J. F. Bauters, M. J. R. Heck, D. John, D. Dai, M.-C. Tien, J. S. Barton, A. Leinse, R. G. Heideman, D. J. Blumenthal, and J. E. Bowers, "Ultra-low-loss high-aspect-ratio Si$_3$N$_4$ waveguides," Opt. Express **19**, 3163–3174 (2011).

6. D. Marpaung, C. Roeloffzen, R. Heideman, A. Leinse, S. Sales, and J. Capmany, "Integrated microwave photonics," Laser Photon. Rev. **7**, 506–538 (2013).
7. Y. Vlasov, W. M. J. Green, and F. Xia, "High-throughput silicon nanophotonic wavelength-insensitive switch for on-chip optical networks," Nat. Photon. **2**, 242–246 (2008).
8. C. Monat, P. Domachuk, and B. J. Eggleton, "Integrated optofluidics: A new river of light," Nat. Photon. **1**, 106–114 (2007).
9. W. Yang, D. B. Conkey, B. Wu, D. Yin, A. R. Hawkins, and H. Schmidt, "Atomic spectroscopy on a chip," Nat. Photon. **1**, 331–335 (2007).
10. G. Calafiore, A. Koshelev, S. Dhuey, A. Goltsov, P. Sasorov, S. Babin, V. Yankov, S. Cabrini, and C. Peroz, "Holographic planar lightwave circuit for on-chip spectroscopy," Light Sci. Appl. **3**, e203 (2014).
11. D. T. Spencer, J. F. Bauters, M. J. R. Heck, and J. E. Bowers, "Integrated waveguide coupled Si_3N_4 resonators in the ultrahigh-q regime," Optica **1**, 153–157 (2014).
12. K. Luke, Y. Okawachi, M. R. E. Lamont, A. L. Gaeta, and M. Lipson, "Broadband mid-infrared frequency comb generation in a Si_3N_4 microresonator," Opt. Lett. **40**, 4823–4826 (2015).
13. J. P. Epping, M. Hoekman, R. Mateman, A. Leinse, R. G. Heideman, A. van Rees, P. J. M. van der Slot, C. J. Lee, and K.-J. Boller, "High confinement, high yield Si_3N_4 waveguides for nonlinear optical applications," Opt. Express **23**, 642–648 (2015).
14. K. Wörhoff, R. G. Heideman, A. Leinse, and M. Hoekman, "TriPleX: a versatile dielectric photonic platform," Adv. Opt. Technol. **4**, 189–207 (2015).
15. Y. Fan, R. M. Oldenbeuving, E. J. Klein, C. J. Lee, H. Song, M. R. H. Khan, H. L. Offerhaus, P. J. M. van der Slot, and K.-J. Boller, "A hybrid semiconductor-glass waveguide laser," Proc. SPIE **9135**, 91351B (2014).
16. Y. Fan, J. P. Epping, R. M. Oldenbeuving, C. G. H. Roeloffzen, M. Hoekman, R. Dekker, R. G. Heideman, P. J. M. van der Slot, and K.-J. Boller, "Optically integrated InP-Si_3N_4 hybrid laser," IEEE Photonics J. **8**, 1–11 (2016).
17. C. G. H. Roeloffzen, L. Zhuang, C. Taddei, A. Leinse, R. G. Heideman, P. W. L. van Dijk, R. M. Oldenbeuving, D. A. I. Marpaung, M. Burla, and K.-J. Boller, "Silicon nitride microwave photonic circuits," Opt. Express **21**, 22937 (2013).
18. J. P. Epping, T. Hellwig, M. Hoekman, R. Mateman, A. Leinse, R. G. Heideman, A. van Rees, P. J. M. van der Slot, C. J. Lee, C. Fallnich, and K.-J. Boller, "On-chip visible-to-infrared supercontinuum generation with more than 495 THz spectral bandwidth," Opt. Express **23**, 19596–19604 (2015).
19. M. A. G. Porcel, F. Schepers, J. P. Epping, T. Hellwig, M. Hoekman, R. G. Heideman, P. J. M. van der Slot, C. J. Lee, R. Schmidt, R. Bratschitsch, C. Fallnich, and K.-J. Boller, "Two-octave spanning supercontinuum generation in stoichiometric silicon nitride waveguides pumped at telecom wavelengths," Opt. Express **25**, 1542–1554 (2017).
20. J. P. Epping, M. Kues, P. J. M. van der Slot, C. J. Lee, C. Fallnich, and K.-J. Boller, "Integrated CARS source based on seeded four-wave mixing in silicon nitride," Opt. Express **21**, 32123–32129 (2013).
21. J. Pfeifle, V. Brasch, M. Lauermann, Y. Yu, D. Wegner, T. Herr, K. Hartinger, P. Schindler, J. Li, D. Hillerkuss, R. Schmogrow, C. Weimann, R. Holzwarth, W. Freude, J. Leuthold, T. J. Kippenberg, and C. Koos, "Coherent terabit communications with microresonator kerr frequency combs," Nat. Photon. **8**, 375–380 (2014).
22. T. Hellwig, J. P. Epping, M. Schnack, K.-J. Boller, and C. Fallnich, "Ultrafast, low-power, all-optical switching via birefringent phase-matched transverse mode conversion in integrated waveguides," Opt. Express **23**, 19189–19201 (2015).
23. C. Xiong, X. Zhang, A. Mahendra, J. He, D.-Y. Choi, C. J. Chae, D. Marpaung, A. Leinse, R. G. Heideman, M. Hoekman, C. G. H. Roeloffzen, R. M. Oldenbeuving, P. W. L. van Dijk, C. Taddei, P. H. W. Leong, and B. J. Eggleton, "Compact and reconfigurable silicon nitride time-bin entanglement circuit," Optica **2**, 724 (2015).
24. T. Ning, H. Pietarinen, O. Hyvärinen, J. Simonen, G. Genty, and M. Kauranen, "Strong second-harmonic generation in silicon nitride films," Appl. Phys. Lett. **100**, 161902 (2012).
25. A. Kitao, K. Imakita, I. Kawamura, and M. Fujii, "An investigation into second harmonic generation by si-rich SiN_x thin films deposited by RF sputtering over a wide range of si concentrations," J. Phys. D: Appl. Phys. **47**, 215101 (2014).
26. J. S. Levy, A. L. Forster Mark A.and Gaeta, and M. Lipson, "Harmonic generation in silicon nitride ring resonators," Opt. Express **19**, 11415–11421 (2011).
27. A. Billar, D. Grassani, M. H. Pfeiffer, S. Kharitonov, T. J. Kippenberg, and C.-S. Brès, "Large second harmonic generation enhancement in Si_3N_4 waveguides by all-optically induced quasi-phase-matching," Nat. Commun. **8**, 1016 (2017).
28. V. Torres-Company and A. M. Weiner, "Optical frequency comb technology for ultra-broadband radio-frequency photonics," Laser Photon. Rev. **8**, 368–393 (2014).
29. U. Österberg and W. Margulis, "Dye laser pumped by Nd:YAG laser pulses frequency doubled in a glass optical fiber," Opt. Lett. **11**, 516–518 (1986).
30. W. Margulis and U. Österberg, "Second-harmonic generation in optical glass fibers," J. Opt. Soc. Am. B **5**, 312–316 (1988).
31. T. Suhara and M. Fujimura, *Waveguide Nonlinear-Optic Devices* (Springer, 2003).
32. www.comsol.com, "COMSOL Multiphysics V5.0," (2014).
33. M. K. Balakirev, L. I. Vostrikova, V. A. Smirnov, and M. V. Entin, "Relaxation of the optical density of glass modulated with bichromatic radiation," J. Exp. Theor. Phys. Lett. **63**, 176–181 (1996).

34. E. M. Dianov, P. G. Kazansky, and D. Y. Stepanov, "Photoinduced effects in optical waveguides," Proc. SPIE **1516**, 81 – 98 (1991).
35. B. Batdorf, C. Krautschik, U. C. Österberg, G. Stegeman, J. W. Leitch, J. R. Rotgé, and T. F. Morse, "Study of the length dependence of frequency-doubled light in optical fibers," Opt. Commun. **73**, 393 –397 (1989).
36. R. H. Stolen and H. W. K. Tom, "Self-organized phase-matched harmonic generation in optical fibers," Opt. Lett. **12**, 585–587 (1987).
37. V. Mizrahi, U. österberg, J. E. Sipe, and G. I. Stegeman, "Test of a model of efficient second-harmonic generation in glass optical fibers," Opt. Lett. **13**, 279 (1988).
38. E. M. Dianov and D. S. Starodubov, "Photoinduced generation of the second harmonic in centrosymmetric media," Quantum Electron. **25**, 395–407 (1995).
39. D. Z. Anderson, V. Mizrahi, and J. E. Sipe, "Model for second-harmonic generation in glass optical fibers based on asymmetric photoelectron emission from defect sites," Opt. Lett. **16**, 796–798 (1991).
40. V. O. Sokolov and V. B. Sulimov, "Formation of electrostatic field gratings in glass by optical and acoustical waves," in "Optics Quebec," (International Society for Optics and Photonics, 1993), pp. 213–222.
41. V. O. Sokolov and V. B. Sulimov, "On the phenomenological theory of the coherent photogalvanic effect in glass," Phys. Status Solidi B **187**, 177–187 (1995).
42. P. Chmela and J. Petráček, "First demonstration of $\chi^{(2)}$ grating encoding function in optical fibers," Opt. Commun. **156**, 374–383 (1998).
43. V. O. Sokolov and V. B. Sulimov, "Theory of third-order nonlinear photoconductivity and third-order photogalvanic effect in glass," Phys. Status Solidi B **187**, 189–204 (1995).
44. M. K. Balakirev, I. V. Kityk, V. A. Smirnov, L. I. Vostrikova, and J. Ebothe, "Anisotropy of the optical poling of glass," Phys. Rev. A **67**, 023806 (2003).
45. M. K. Balakirev and V. A. Smirnov, "Kinetics of photoinduced optical anisotropy in oxide glass," J. Exp. Theor. Phys. Lett. **77**, 217–220 (2003).
46. M. M. Fejer, G. A. Magel, D. H. Jundt, and R. L. Byer, "Quasi-phase-matched second harmonic generation: tuning and tolerances," IEEE J. Quant. Electron. **28**, 2631–2654 (1992).
47. R. W. Boyd, *Nonlinear Optics* (Academic Press, 2013).
48. W. L. Warren, J. Robertson, and J. Kanicki, "Si and N dangling bond creation in silicon nitride thin films," Appl. Phys. Lett. **63**, 2685–2687 (1993).
49. J. Robertson, W. L. Warren, and J. Kanicki, "Nature of the Si and N dangling bonds in silicon nitride," Journal of Non-Crystalline Solids **187**, 297–300 (1995).
50. D. T. Krick, P. M. Lenahan, and J. Kanicki, "Electrically active point defects in amorphous silicon nitride: An illumination and charge injection study," J. Appl. Phys. **64**, 3558–3563 (1988).
51. E. M. Dianov, P. G. Kazanskii, and D. S. Starodubov, "Transient gratings of a quadratic nonlinear susceptibility due to the coherent photogalvanic effect in semiconductor-microcrystallite-doped glasses," Quantum Electron. **24**, 632–635 (1994).
52. G. I. Stegeman, D. J. Hagan, and L. Torner, "$\chi^{(2)}$ cascading phenomena and their applications to all-optical signal processing, mode-locking, pulse compression and solitons," Opt. Quantum Electron. **28**, 1691–1740 (1996).
53. G. F. R. Chen, T. Wang, C. Donnelly, and D. T. H. Tan, "Second and third order dispersion generation using nonlinearly chirped silicon waveguide gratings," Opt. Express **21**, 29223 (2013).
54. J. Čáp and P. Chmela, "Self-organized parametric down conversion and photoinduced reflectivity in optical fibers," Opt. Quantum Electron. **35**, 1079–1090 (2003).
55. H. R. Telle, G. Steinmeyer, A. E. Dunlop, J. Stenger, D. H. Sutter, and U. Keller, "Carrier-envelope offset phase control: A novel concept for absolute optical frequency measurement and ultrashort pulse generation," Appl. Phys. B **69**, 327–332 (1999).
56. D. J. Jones, S. A. Diddams, J. K. Ranka, A. Stentz, R. S. Windeler, J. L. Hall, and S. T. Cundiff, "Carrier-envelope phase control of femtosecond mode-locked lasers and direct optical frequency synthesis," Science **288**, 635–639 (2000).
57. A. S. Mayer, A. Klenner, A. R. Johnson, K. Luke, M. R. E. Lamont, Y. Okawachi, M. Lipson, A. L. Gaeta, and U. Keller, "Frequency comb offset detection using supercontinuum generation in silicon nitride waveguides," Opt. Express **23**, 15440 (2015).

1.   Introduction

Photonic integrated circuits (PICs) realized with various different material platforms, *e.g.*, SOI (silicon on insulator) [1, 2], InP [3, 4], polymers [3], SiO$_2$ [2, 3] and SiN [5, 6], have gained a tremendously growing importance in modern photonic technologies. This is due to a huge variety of emerging applications in high-throughput communications [7], optical sensing [8] and the life sciences, the latter, specifically, when involving visible light [9, 10]. Semiconductor waveguide platforms offer the strongest first-order, i.e., linear, optical interactions, such as required for light generation, amplification or photo detection. Dielectric waveguide platforms, on the other hand, provide lowest propagation loss and tolerate high intensities, thereby enabling various types of

optical functionalities via nonlinear optical interactions.

A most prominent example is photonic circuits fabricated from stoichiometric Si_3N_4 grown via low-pressure chemical vapor deposition (LPCVD), embedded in a SiO_2 cladding. This platform offers a unique combination of adjustable properties, *i.e.*, record-low propagation loss (<0.001 dB/cm) [5] such as for high-Q resonators [11], a wide spectral range of optical transparency (from about 310 nm throughout the entire visible spectrum up to 5.5 μm [12]), and a high index contrast to achieve tight mode confinement. The latter is achieved with extremely thick waveguide cores, fabricated with a novel approach of stepwise filling of pre-etched grooves [13]. This platform has also reached a considerable degree of maturity, allowing two-dimensional tapering [14] for low-loss fiber coupling or realizing hybrid lasers [15, 16]. The platform supports also a wide range of optical functionalities [11, 17] by offering various different core cross sections for waveguide dispersion engineering, and offers a highly reproducible material dispersion [13, 14]. Regarding third-order nonlinearities, the recent demonstration of the broadest-ever optical spectrum generated on a chip, 495 THz when pumped at 1064 nm [18], shifted more towards the mid-infrared when pumped at 1550 nm, while still maintaining a bandwidth of 453 THz [19]. This has opened a wide prospective towards four-wave mixing [20], frequency comb generation [21] and all-optical switching [22].

Additional functionalities that can be used with lower field strengths would become accessible if this platform would as well provide a second-order nonlinear response, for instance for electro-optic modulation, second-harmonic generation (SHG), or parametric down-conversion. Such nonlinearity, having as its signature a non-zero second-order susceptibility, is also of interest for generating quantum correlated photon pairs directly within reconfigurable time-bin entanglement circuits [23].

A fundamental precondition for making use of such second-order nonlinearity is, however, that the material provides a non-inversion symmetric structure. With the discussed silicon nitride platform, this is a problem because the involved materials, Si_3N_4 and SiO_2, are amorphous and thus inversion symmetric. On the other hand, there have been four reports on second-order response in related amorphous SiN-type materials. Specifically, second-harmonic generation has been observed in SiN films (fabricated using plasma enhanced chemical vapor deposition [24] or fabricated with RF sputtering [25]), in Si_3N_4 ring resonators (fabricated with plasma enhanced chemical vapor deposition at lower temperatures [26]) where the nanoscale structure of the waveguide breaks the inversion symmetry and modal phase matching is employed, and in Si_3N_4 waveguides fabricated using stress release patterns [27] where, similar to our work, the coherent photogalvanic effect breaks the inversion symmetry. However, we find an equivalent second-order response that is an order of magnitude larger. Differences in fabrication are important to note because both the Si to N ratio as well as the type of fabrication process have a strong influence on the size of the optical bandgap, the propagation losses and the third-order nonlinear response [28]. The stoichiometric, low-loss Si_3N_4 material waveguides described above have not been investigated so far for their second-order nonlinear response, thus leaving open whether functionalities based on a non-zero $\chi^{(2)}$ susceptibility can be realized.

Here we present the first observation of a second-order response in such LPCVD-grown, stoichiometric Si_3N_4 waveguides, using second-harmonic generation. Employing a mode-locked laser at a wavelength of 1064 nm delivering 6.2 ps pulses and coupling an average power of 13 mW into a waveguide with $0.9 \times 1\ \mu m^2$ cross-section and 36 mm length, a second-harmonic (SH) output of 53 μW was reached, which corresponds to a conversion of 0.4%, with an equivalent second-order nonlinear susceptibility of 3.7 pm/V. We observed that in order to generate a SH output, an optical initialization process is required, similar to what had been observed earlier in glass fibers [29, 30]. The process involves exposing the waveguides with the in-coupled IR pulses at mW power levels over time intervals between several minutes to hours, depending on the infrared power.
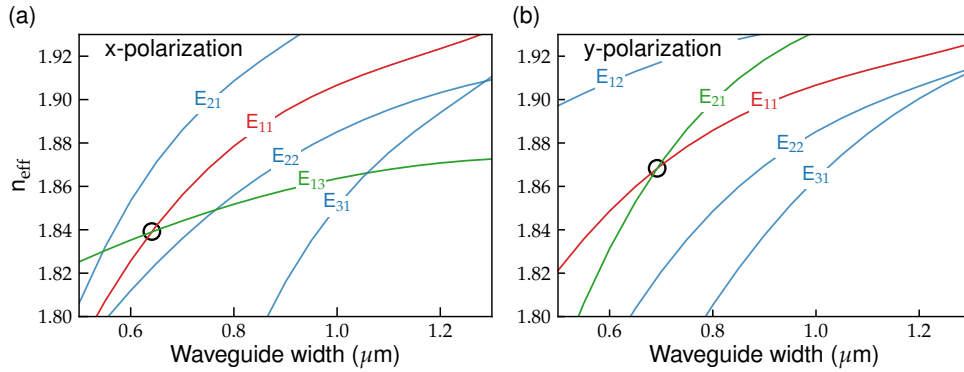
Fig. 1. **(a)** Calculated effective refractive index *vs.* waveguide width, *w*, for the IR fundamental mode (E_{11}) with quasi-horizontal polarization (red curve), and for various transverse modes at 532 with quasi-horizontal polarization. The waveguide height is fixed at 1 μm. **(b)** Analogous calculation of dispersion for quasi-vertically polarized modes. The black circles indicate where modal phase matching is expected, namely with $w = 0.65$ μm or 0.68 μm.

2. Experimental procedure and results

In our experimental approach we aimed on demonstrating second-harmonic generation based on modal phase matching [31]. This requires the identification of proper waveguide dimensions that provide the same effective refractive index (waveguide index) for propagation at the fundamental and second-harmonic frequencies. To calculate the effective refractive index dispersion, $n_{\text{eff}}(\omega)$, as function of the width and height of the waveguide core we use a fully vectorial finite-element mode solver [32] with the Sellmeier dispersion data given by Luke *et al.* [12] for the wavelength range of the available pump laser (around 1.064 μm wavelength) and its second-harmonic (around 532 nm). For maximizing the waveguide-internal intensity via a strong confinement, enlarged core cross-sections are considered with a height and width around 1 μm. The two-dimensional step-index profile used for the calculations is based on the actual waveguide shape available from SEM images [13], which has slightly rounded edges at the bottom. Eigenmode calculations have shown that these rounded edges do not affect the polarization of the eigenmodes.

Figure 1 gives an overview of the calculated effective index, n_{eff}, *vs.* the waveguide width, *w*, for a constant waveguide height, *h*, of 1 um for two polarizations. The effective refractive index for the fundamental guided mode of the infrared (IR) pump light (labeled E_{11}), at a vacuum wavelength of 1064 nm, is shown as red curves. The effective refractive index of the next-higher transverse modes, E_{ij}, of the according second-harmonic at 532 nm wavelength is shown as green and blue curves, for quasi-*x* (horizontally) and quasi-*y* (vertically) polarized light (Figs. 1(a) and 1(b), respectively). It can be seen that modal phase matching involving the E_{11} mode and a given polarization is expected only for a single, specific waveguide width where the IR dispersion curve crosses a specific SH dispersion (green) curve as indicated with a black circle. According to the calculations, phase matching is expected with a waveguide width of about $w = 0.65$ μm for the horizontally polarized transverse mode E_{13}, and about $w = 0.68$ μm for the vertically polarized transverse mode E_{21}.

Figure 2 shows the experimental setup employing a mode-locked Yb-fiber laser operating at a wavelength of 1064 nm with a pulse duration of 6.2 ps and a repetition rate of 20 MHz (Toptica, PicoFYb 1064). The power of the laser and its polarization was controlled via two half-wave plates and a polarizing beam splitter. To maximize the input coupling, the round cross-section provided by the laser in a collimated beam was reduced from 4 mm to 2.5 mm with a telescope
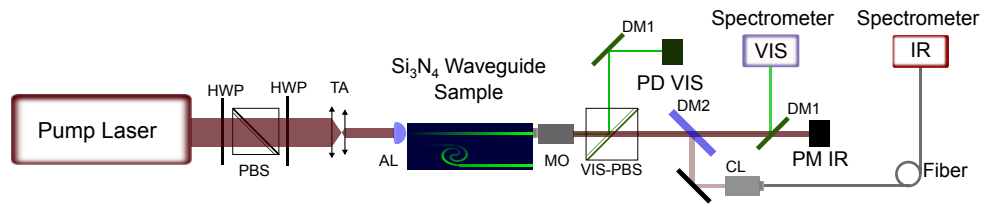
Fig. 2. Schematic of the experimental setup used for second-harmonic (SH) generation in Si$_3$N$_4$ waveguides. The infrared pump laser with a wavelength near 1 μm is sent through two half-wave plates (HWP), through a telescope arrangement (TA), and a polarizing beam splitter (PBS) and focused into a waveguide sample with an aspheric lens (AL). Output from the waveguide is collected with a microscope objective (MO). A polarizing beam splitter (VIS PBS) for the SH light and transparent for the IR pump light is used as analyzer and to separate the SH output from the IR pump light. The SH output is directed to a photodiode (PD VIS) via a dichroic mirror (DM1) for further suppression of any residual IR pump light. The transmitted IR pump light, together with about 1% residual transmitted SH light, is directed towards a infrared power meter (PM IR). Part of the transmitted IR pump power is sampled (16%) by a dichroic mirror (DM2) and send into an infrared spectrometer (IR) using a collection lend (CL) and a large mode area fiber. A second dichroic mirror (DM1) separates the residual transmitted SH light from the IR path and sends it to the spectrometer for visible light (VIS).

arrangement. Due to the high confinement of IR light in the waveguide, with a calculated effective mode area of around 0.5 μm^2, achieving maximally efficient input coupling would require a rather high numerical aperture ($NA \approx 1.25$) whereas, due to availability, we used an aspheric lens with moderate numerical aperture ($NA = 0.68$, Thorlabs C330TMD-C). With this arrangement, the input power coupling loss estimated from throughput measurements amounted to about 75%, assuming a propagation loss of 0.5 dB/cm [13] inside the waveguide. The output light from the other waveguide facet was collected via a microscope objective ($NA = 0.74$, Mitutoyo x60) with an estimated output power coupling loss of 43% for the fundamental (as obtained from the measured collimated output from the microscope objective and power measurements with a large area power meter). A polarizing beam splitter with an extinction ratio of 100:1 for the SH light and transparent for the IR light is placed behind the collecting microscope object to analyze the polarization state of the generated SH light and functions as a first separator of the SH light from the IR light. The SH light is then sent to a photodiode for power measurement via a dichroic mirror for further suppression of any residual IR light. The light transmitted by the polarizing beam splitter consists of the IR light and 1% of residual SH light. The IR light is send to an infrared power meter. A small fraction (16%) was sampled using a dichroic mirror (DM2) and directed toward a spectrometer for infrared light. A second dichroic mirror (DM1) is used to separate the residual transmitted SH light from the IR light and sends it toward a spectrometer for visible light. The fundamental and SH powers were continuously monitored *vs.* time. Details about the manufacturing of the large core area waveguides used in our experiments are given by Epping *et al.* [13] and are based on the proprietary TripleX process from LioniX International.

In Figs. 3(a)-3(d) several typical examples of time dependent measurements performed during the initialization are shown, *i.e.*, when exposing the waveguides to pump radiation for the first time. The examples comprise two different waveguide widths ($w = 0.9 \mu$m and 1.2 μm), and three different waveguide lengths ($L = 74, 60$ and 22 mm). The power of the waveguide-internal pump laser, in these examples using horizontally polarized light, is shown as red traces and was kept constant after turn-on. The traces shown in green display the generated SH *vs.* time. It can be seen that the SH output does not appear simultaneously with the pump laser turn-on. Instead, the SH builds up with a delay of minutes to hours, after which it rises within tens of seconds to

minutes until reaching a steady state, with the sooner and steeper growth occurring at higher pump powers.

For comparison with the experimental data we applied a least-square fit using the exponential growth function as given in [33], $f(t) = \frac{a}{1+(Rt_0-1)\,e^{-2tR}}$, where a, t_0 and R are fit parameters. In this expression, a is the steady-state value, t_0 is the delay time and R quantifies the growth rate of the SH output, *i.e.*, the steepness of the slope at the moment that the output reaches a $1/e$-fraction of the steady-state value. The figure shows that, for all pump powers, the fit function matches the experimental data very well. For an evaluation of the power dependence, the values for the growth rate retrieved from the fits are displayed as data points in Fig. 3(e) *vs.* the pump power, P_p. For a comparison, we used a least-square fit of a linear function of the pump power as $R = (P_p - P_0)/F$, where F and P_0 are fit parameters. P_0 is the pump power where the growth rate becomes zero, indicating the existence of a minimum or threshold pump power required to obtain SHG. Figure 3(e) shows that the fit agrees well with the measured growth rates, indicating a linear dependence of the growth rate R on the average IR pump power that is independent of the dimensions of the waveguide. The threshold pump power retrieved from the fit, $P_0 = 1.22$ mW, is indicated in Fig. 3(e) with an arrow.
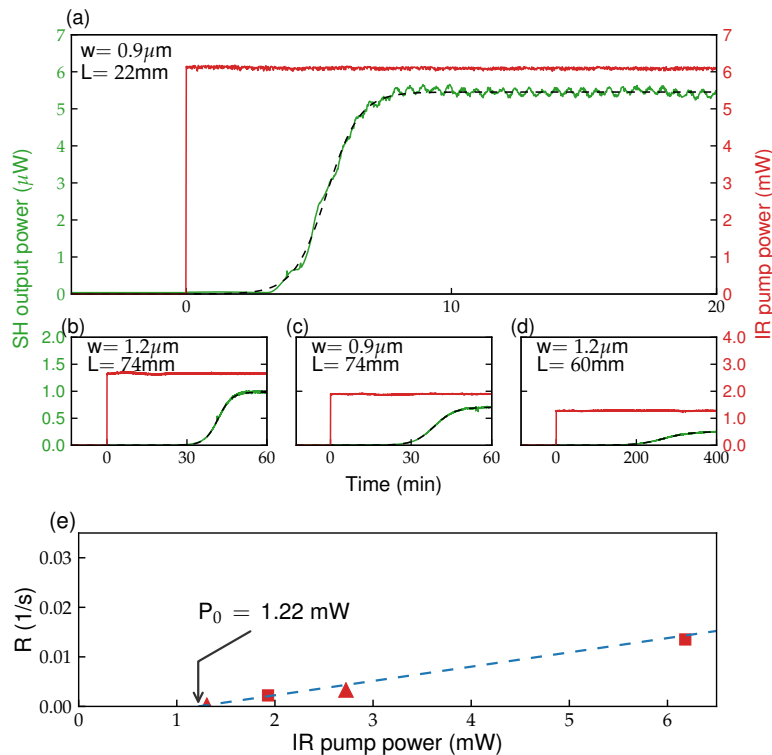

Fig. 3. (a) to (d). Initial growth of the second-harmonic output power *vs.* time (green traces) in four waveguides of different widths, w, and lengths, L. The red traces show the average infrared pump power in the waveguide. The dashed curves are least-square fits of the exponential function $f(t)$ (see main text) to the experimental data. (**e**). Shown is the rate of growth, R, where the SH output has reached a 1/e-fraction of its steady-state value, as retrieved from the fits to the data in (a-d), *vs.* the waveguide-internal pump power. The triangular and square symbols represent growth rates as obtained with waveguide widths of $w = 0.9$ μm and 1.2 μm, respectively. The dashed curve is a linear least-square fit to the data.

In order to verify that the observed green output is indeed SHG and not radiation from a different process, such as fluorescence from impurity ions, the SH output power was measured *vs.* the IR pump power. Expected is a quadratic growth with the pump power and that the output shows a well-defined polarization. The experiment was carried out by reducing the pump power towards zero, starting from the value that was used to generate a steady-state SH output, and also by increasing it from zero back to the maximum available power. In these measurements, performed after the initialization as described above, we observed that the SH power followed the pump power reduction or increase without any noticeable delay (sampling time 1 s). Also, the output was found linearly polarized, parallel to the polarization of the pump laser. The measured SH output *vs.* pump power is displayed in Fig. 4. A double-logarithmic plot is chosen for easy identification of power laws, where a quadratic dependence shows as a straight line with a slope, m, of 2. The dashed line shown in the figure is a least-square fit with a fixed slope of $m = 2$ and with a variable offset as single fit parameter. It can be seen that the generated output power follows very well the expected quadratic dependency of second-harmonic generation. The agreement clearly proves that the investigated waveguides show a second-order nonlinear response.
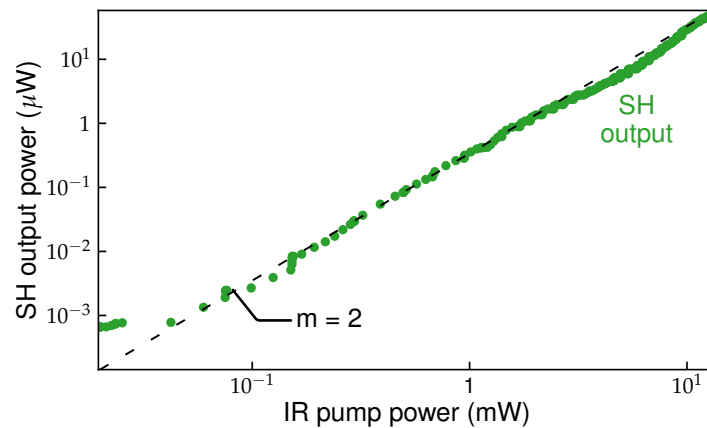

Fig. 4. Measured second-harmonic (SH) output as function of input infrared pump power. The used waveguide has a width of 0.9 μm, a height of 1.0 μm and a length of 22 mm. The dashed line is a quadratic fit curve (slope $m = 2$).

In order to investigate whether the generated output involves components also of higher-order nonlinear response, specifically, self-phase modulation or four-wave mixing via the $\chi^{(3)}$-nonlinear susceptibility, we recorded the power spectra of the pump laser and the SH output for comparison with each other. If the output is solely dependent on the pump power with a square-law, one expects that the spectral shape of the SH output should match the convolution of the IR spectrum with itself (autocorrelation of the IR power spectrum). Figure 5 compares an example of a measured and normalized power spectrum of the SH (green trace) with the normalized autocorrelation spectrum of the measured pump spectrum (red trace). It can be seen that the SH power spectrum fits the autocorrelated pump spectrum well, which excludes noticeable spectral influences of self-phase modulation and four-wave mixing.

A next measurement was performed to attempt clarifying what type of phase-matching mechanism was present that enables generation of the observed SH. Figure 1 suggests that modal phase matching should be possible only with a single, specific value for the waveguide width. The experiments, however, showed that SH output is generated regardless of the waveguide width, such that equal phase velocities of transverse modes alone cannot explain the observed phase
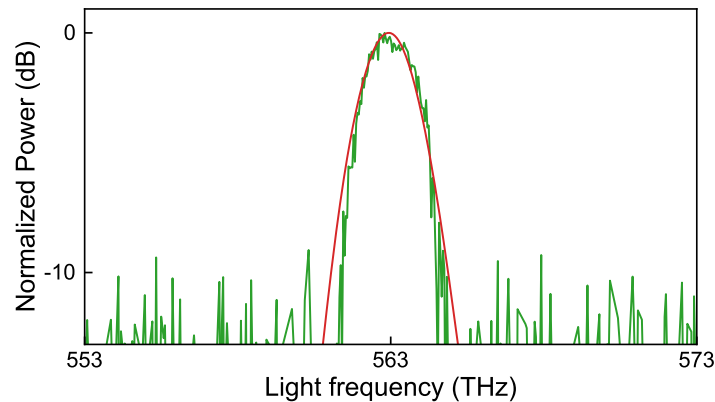
Fig. 5. Power spectra of the generated visible radiation (green trace) compared with the autocorrelated infrared pump power spectrum (red trace) in a logarithmic plot, with peak values normalized to 0 dB. The SH was generated in a waveguide with a 0.6×1 μm2 cross-section and a length of 36 mm, with a waveguide-internal pump power of 4.8 mW.

matching. For instance, SHG is observed with $w = 0.9$ μm as well as with 1.2 μm (see Fig. 3 and also Fig. 7(a)). To gain further information by identifying the spatial mode in which the SH is generated, we recorded the transverse intensity profile of the visible output in the far-field behind the waveguide, with a microscope objective and a CCD. To provide a large *NA* for the recording, a microscope objective was placed (*NA* = 1.4, 60x, *Zeiss*) with immersion oil (index of 1.5) slightly closer than the focal distance, in order to maintain a diverging beam for a far-field measurement.

The CCD was positioned about 1 m beyond the microscope objective. The measured SH far-field intensity profile, normalized to the maximum intensity, for a waveguide with a cross-section of 0.7×1 μm2 and length of 36 mm is shown in Fig. 6(a). Figure 6 shows a transverse-moded structure with vertically three main lobes (the lower one and the higher one having the highest intensity, the central one distorted), and with horizontally two weaker side lobes. As the SH intensity profile could only be measured in the far-field, it is not possible to determine the modal decomposition of the SH to great detail. Further complications are some diffraction by the objective aperture and possible asymmetries introduced by the meniscus of the oil droplet present between waveguide facet and microscope objective. Asymmetries became clearly visible in the experiment when the objective was moved too far from the exit facet of the waveguide. However, the main features in the measured pattern, such as number of lobes and symmetry, allows the identification of the main mode in which the SH is generated.

To that end, Figs. 6(b)-6(d) show the normalized intensity profiles of the waveguide modes E_{13}, E_{21} and E_{31}, respectively, for the horizontal polarization. In calculating the transverse profiles of these eigenmodes, the actual waveguide geometry as determined from SEM measurements was used [13]. The waveguide core has rounded edges at the bottom, *i.e.*, at the location of minimum y value in Fig. 6, and this asymmetry is responsible for the higher intensity of the lower lobes in the profiles shown in Fig. 6. Qualitatively, the presence of a weak central spot with vertically stronger and horizontally weaker side spots, the highest similarity was found with the E_{13} mode, with some small contributions from either the E_{21} mode, the E_{31} mode or both. For reasons discussed below, we also expect that the SH radiation is dominantly generated in the E_{13} mode for this waveguide.

Finally, in order to identify the optimum overall conditions for SHG we recorded the dependence
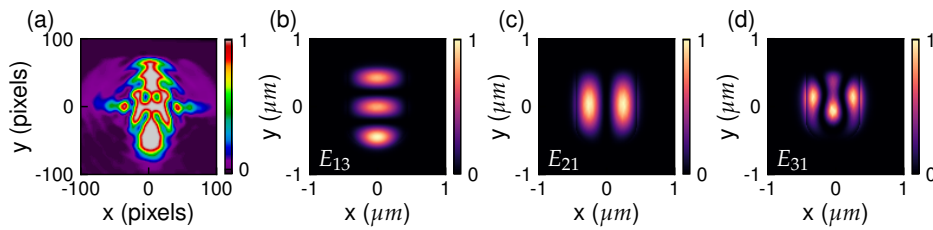
Fig. 6. Far-field intensity pattern formed by the second-harmonic output beam, normalized to the maximum intensity, recorded with a CCD behind an immersion objective **(a)** and calculated normalized intensity pattern for the waveguide modes E_{13} **(b)**, E_{21} **(c)** and E_{31} **(d)**. The waveguide has a width of 0.7 μm and a height of 1 μm. The SH output and waveguide modes are horizontally polarized.
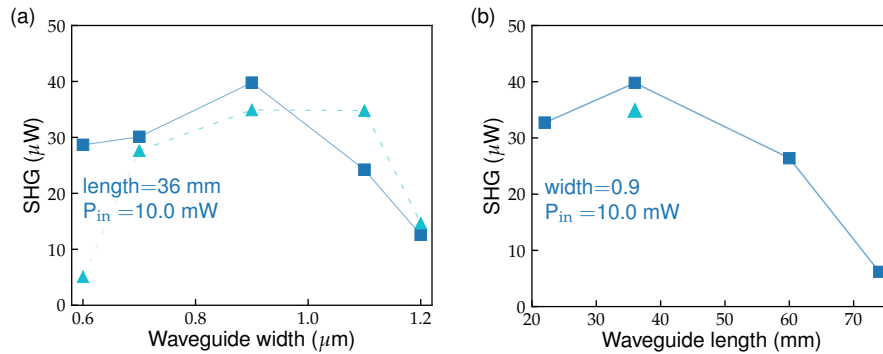

Fig. 7. **(a)** Measured second-harmonic (SH) output power for different waveguide widths with a fixed input power of 10 mW, horizontally polarized (squares) and vertically polarized light (triangles) for a waveguide length of 36 mm. **(b)** Measured second-harmonic power for different waveguide lengths with a fixed input power of 10 mW, for a waveguide with 0.9×1 μm^2 cross-section.

of the SHG output *vs.* the waveguide width, length, and polarization. Figure 7(a) shows the measured power for five different waveguide core widths, 0.6, 0.7, 0.8, 0.9, 1.1, and 1.2 μm (height of 1 μm and length of 36 mm), using the same waveguide-internal pump power of 10 mW. Squares represent horizontally polarized light and triangles vertically polarized light. Figure 7(b) shows the SH output power as a function of the waveguide length using a fixed waveguide core cross-section (0.9×1 μm^2) and the same waveguide-internal pump power (10 mW).

A maximum SH output is found for a waveguide length of $L = 36$ mm, and a cross-section of 0.9×1 μm^2 for horizontally polarized pumping. This corresponds to a conversion efficiency of 0.4%. Beyond this length, Fig. 7(b) shows a decrease in SH power, similar to what is observed for SHG in glass fibers [34,35]. Regarding polarization, two effects were observed when changing the input polarization. Initially, *i.e.*, immediately after injecting the other polarization, there was no SH output. Instead, a SH build-up took place with a certain delay and growth rate as described in Fig. 3. Thereafter, the SH output followed instantaneously any variation of the pump power. The second observation is that the polarization of the SH output was always parallel to that of the pump

radiation. Independent of polarization effects it was observed that the second-order nonlinear response became erased when illuminating the waveguide with UV radiation (a PR-100, UVP Inc., with a 254 nm wavelength was used for ten minutes). After storing initialized waveguides in complete darkness at room temperature, typically for at least a week, we did not observe any degradation of the nonlinear response.

In order to verify the reproducibility of our observations, we have repeated some measurements using waveguides with equal dimensions from different sections of the wafer. These measurements include writing the charge grating (*c.f.* Fig. 3) and the dependence of second harmonic power on the IR pump power (*c.f.* Fig. 4). In all cases investigated, the measurements reproduced within the experimental accuracy.

3. Discussion

The most basic expectation that the second-harmonic (SH) output power would follow a quadratic growth with the input pump power, and that the spectrum would have the same spectral bandwidth and shape as the autocorrelated pump spectrum, is confirmed by the experimental observations. However, contrary to what is expected, which is the absence of SH output, due to fabrication as amorphous materials, we observed second-harmonic generation, though this required an initialization process during which the SH is time dependent. This time dependency is a growth over time of the SH power towards a steady-state value, as long as the pump power is above a threshold value (P_0 as indicated in Fig. 3(e)). Unexpected is also that SHG was observed in all of the investigated waveguides, independent of their width, which excludes an explanation solely based on modal phase matching. Instead, during the initialization, an additional wave-vector, *i.e.*, a matching spatial periodicity, appears to become available that compensates the remaining wave vector mismatch of modal phase matching.

We address our observation of phase-matched SHG to the so-called coherent photogalvanic effect (CPGE), because of the excellent match of the fit functions to the measured temporal growth function and growth-rate *vs.* power dependence in Figs. 3(a)-3(e). The temporal fit function was derived by Balakirev *et al.* [33] for the CPGE in glass. The first observations of the CPGE in guided optics were made with phosphor-doped silica fibers [29, 30, 36–38] and several phenomenological models were proposed [33, 39–42].

In brief, a first part of the CPGE is related to the third-order term in the expansion of Ohm's law, $\vec{j} = \sigma \vec{E}$, in powers of the electric field [43]. Here, $\vec{j}$ is the current density, σ is the conductivity and $\vec{E}$ a directed (DC) electric field generated by the light fields present in the waveguide. A second, underlying nonlinear effect is third-order optical rectification, which originates from the simultaneous presence of light at the fundamental frequency, ω, and its second harmonic, at 2ω. The $\chi^{(3)}$-nonlinear rectification field induces a photocurrent density that is proportional to $\vec{E}(\omega)\vec{E}(\omega)\vec{E}^*(2\omega)$. This nonlinear DC current density possesses a spatial periodicity set by the wavenumber mismatch between the fundamental and second-harmonic fields ($\Delta k = 2k(\omega) - k(2\omega)$). The current density leads to a spatial redistribution of electrons between long-lived intra-band trap sites [38, 39, 44], which is the origin for generating an effective second-order nonlinearity. An equivalent picture is the creation of a nonlinear conduction via multi-photon excitation of electrons into the conduction band. Simultaneously, the optical rectification field created via the third-order susceptibility creates a charge relocation between the trap sites with a spatial pattern that provides self-organized quasi-phase matching.

For a somewhat more detailed description, we make the simplification that all optical fields have the same linear polarization, in agreement with our experimental observation. The third-order nonlinear conductivity and susceptibility tensors are assumed to be isotropic and can be represented as scalars as the materials under consideration are amorphous. Accordingly, we treat all fields, current densities and tensors as scalar quantities.

We define the electric field of the fundamental input wave as

$$E(\omega; \vec{r}) = A_1(z)E(\omega; x, y)cos(k(\omega)z + \varphi_1), \tag{1}$$

and the second-harmonic field as

$$E(2\omega; \vec{r}) = A_2(z)E(2\omega; x, y)cos(k(2\omega)z + \varphi_2). \tag{2}$$

Here, z is the propagation coordinate, $k(\omega)$ and $k(2\omega)$ are the wavenumber of fundamental and SH, and φ_1 and φ_2 are phase offsets for the fundamental and SH fields. $A_1(z)$ and $A_2(z)$ are the amplitudes of the field distributions along the propagation direction for the fundamental and the SH waves, $E(\omega; x, y)$ and $E(2\omega; x, y)$ represent the transverse field distributions, respectively.

Electrons, promoted to the conduction band via multi-photon absorption, are driven away from their original locations by a static (DC) electric field, E_{DC}, that is generated via the third-order nonlinearity (third-order optical rectification),

$$P^{(3)}_{DC}(0; \vec{r}) = \frac{3}{8}\varepsilon_0\chi^{(3)}(0 = \omega + \omega - 2\omega)E(\omega; \vec{r})E(\omega; \vec{r})E^*(2\omega; \vec{r}). \tag{3}$$

Equation (3) shows that the optical rectification field exhibits a spatial modulation set be the wavevector mismatch between the fundamental and second harmonic fields that is contained in the z-dependence of $E(\omega; \vec{r})$ and $E(2\omega; \vec{r})$. Consequently, the associated nonlinear photocurrent density j_{ph} given by [38, 45]

$$j_{ph}(\vec{r}) = C(x, y)|A_1(z)|^2 A_2(z)|E(\omega; x, y)|^2 E^*(2\omega; x, y) \cos(\Delta k z + \Delta\varphi) \tag{4}$$

exhibits the same spatial modulation. In Eq. (4), $C(x, y)$ is the effective photogalvanic coefficient [41, 43, 45], $\Delta k = 2k(\omega) - k(2\omega)$ is the wavenumber mismatch, and $\Delta\varphi$ is a constant. The direction of the current follows the transverse polarization of the inducing light fields. Via this photocurrent and due to the presence of trap-sites, a long-lived charge grating is written into the material which remains present when the optical fields are turned off, which can be viewed as an optical poling effect [44].

In the presence of light, the charge grating continues to develop, but the development ceases when the transversely oriented space-charge field, $\mathcal{E}_{DC}$, associated with the charge grating balances the optical rectification field,

$$\varepsilon_0\chi^{(1)}\mathcal{E}_{DC} = -\varepsilon_0\chi^{(1)}E_{DC} = -P^{(3)}_{DC}(0; \vec{r}). \tag{5}$$

Alternatively expressed, the development of the charge grating will cease when the space-charge field has increased to a level where

$$\mathcal{E}_{DC}(\vec{r}) = -j_{ph}(\vec{r})/\sigma_{\text{eff}}, \tag{6}$$

where σ_{eff} is the effective conductivity of the material in the presence of the optical fields. This conductivity is composed of the third-order nonlinear conductivity $\sigma^{(3)}$ and of a background conductivity, also named dark conductivity, which has a low value for the case of amorphous glass [41]. The spatial period of $\mathcal{E}_{DC}(\vec{r})$ along z is again given as Eq. (4) by the fundamental *vs.* SH wavenumber mismatch.

Finally, the fundamental light field, $E(\omega, \vec{r})$, together with the static field, $\mathcal{E}_{DC}$, generates a second-harmonic polarization via the material's third-order nonlinear response, of which the transverse component is given by

$$\mathcal{P}^{(3)}(2\omega; z) = \frac{3}{8}\varepsilon_0\chi^{(3)}(z)\mathcal{E}_{DC}(\vec{r})E(\omega; \vec{r})E(\omega; \vec{r}). \tag{7}$$

This third-order response at the second-harmonic frequency can be seen as an effective second-order polarization based on an effective second-order nonlinearity, as given by [38]

$$\chi_{\text{eff}}^{(2)}(\vec{r}) = 3\chi^{(3)}\mathcal{E}_{DC}(\vec{r}). \tag{8}$$

In Eq. (8), the induced $\mathcal{E}_{DC}$, and thus also $\chi_{\text{eff}}^{(2)}$ assumes the form of a spatial grating along z with the periodicity set by Δk. The spatial structure of $\chi_{\text{eff}}^{(2)}$ is then similar to a periodically poled second-order nonlinear crystal that provides quasi-phase matching [46], in this case for second-harmonic generation.

Phenomenological description of second harmonic mode selection

As described above, the CPGE provides quasi-phase matching independent of the wavenumber mismatch. Therefore, a second-harmonic output should be generated independent of the chosen waveguide width which was indeed experimentally observed. However, for the same reason, the generation should then also be possible independent of the specific type of transverse mode in which the second-harmonic field is generated. For instance, SHG should also be generated in the fundamental mode, $E_{11}(2\omega)$ by the fundamental IR mode, $E_{11}(\omega)$. In contrast to this, we have observed the SH output to be generated predominantly in a specific higher-order (transverse) mode shown in Fig. 6(a), *i.e.*, in the E_{13} mode (Fig. 6(b)) with only some small E_{21} (Fig. 6(c)) or E_{31} (Fig. 6(d)) modes. This rises the question, why the dominant SH mode is E_{13}. In order to discuss possible reasons, in the following we present a phenomenological description of details in the generation of the spatial charge distribution expected in our case.

To generate an initial photocurrent via an optical rectification field, an initial SH seed wave is required. Initially, the seed wave might posses only a small amplitude. Nevertheless, the nonlinear feedback, enabled by the photocurrent-generated charge grating responsible for the effective second-order nonlinearity that leads again to second-harmonic generation, will eventually lead to an exponential growth starting from the seed wave. An initial SH seed wave can be present, *e.g.*, from surface SHG near the interface between core and cladding [47], near local material anisotropies [39], or by photoionization of defects, *i.e.*, of electrons from dangling bonds [43, 48].

Two mechanisms can be responsible for the nonlinear optical generation of a conductivity, required for the coherent photogalvanic effect. The first possibility is excitation of electrons via three-photon absorption from the valance band to the conduction band [44]. This possibility is, however, not likely in our experiments since the bandgap of stoichiometric Si_3N_4 (4.9 eV) is even larger than the energy of four pump photons (4.6 eV). The second mechanism is via dangling bonds in stoichiometric silicon nitride, which can be created via absorption of three pump photons [49]. Note for a longer wavelength pump laser, *e.g.*, at 1550 nm, a three-photon absorption process would not bring the absorbed energy above the threshold for creating the dangling bonds. In LPCVD Si_3N_4 two main types of dangling bonds are possible, silicon (K-centers, having an energy of ~2.6 eV above the upper edge of the valence band) and nitrogen (N-centers, having an energy of ~0.3 eV above the upper edge of the valence band) [50]. These dangling bonds allow photoexication of electrons into the conduction band. As the dangling bond defects are most stable in their charged state [49] they also act as trap sites and provide the mechanism to create long-lived charge gratings in the core of the waveguide. An established charge grating can be neutralized by detrapping of the charges, *e.g.*, via absorption of UV radiation or heating of the waveguide [48]. Depletion of available trap sites may be one reason for saturation of the SH radiation shown in Fig. 7(b). However, other mechanisms may also play a role, especially absorption and processes that affect the relative phasing of the fundamental and second harmonic fields and the $\chi_{\text{eff}}^{(2)}$ grating. For example, when $\chi_{\text{eff}}^{(2)}$ is written in the presence of a seed SH field, it is found that the SH generated by the grating is not in phase with $\chi_{\text{eff}}^{(2)}$ and this saturates the magnitude of the $\chi_{\text{eff}}^{(2)}$ that can be generated [34, 36].
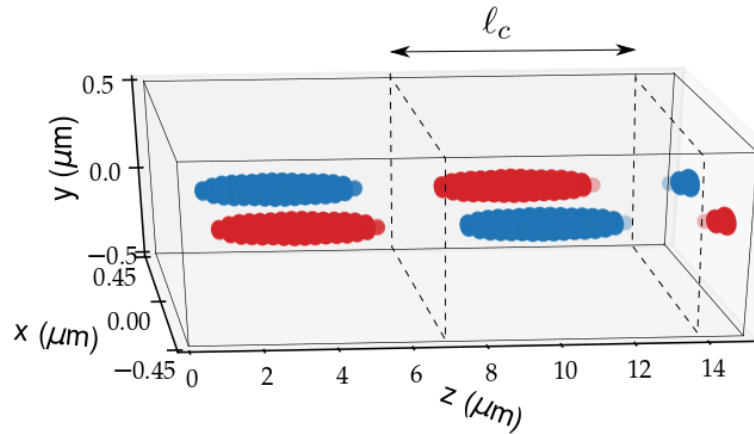
Fig. 8. Normalized charge distribution in the waveguide core induced by the coherent photogalvanic effect. The generating optical fields are assumed to be the fundamental mode $E_{11}(\omega; \vec{r})$ for the IR field and the $E_{13}(2\omega; \vec{r})$ mode for the SH field, both polarized along the x-direction. For clarity only charge values with $|\rho|$ above 80% of the maximum value are plotted, where red and blue represents positive and negative charge, respectively. The sign of the effective $\chi^{(2)}$ is then given from blue to red. The horizontal arrow indicates the coherence length for SHG, $\ell_c = \frac{\pi}{\Delta k}$, in absence of quasi-phase matching.

The establishment of the charge grating may be described and understood as follows. The time dependency of the SH output is dominated by the excitation of charges by the pulsed laser (ps timescale), while the recombination time of charges to a vacancy is rather long ($\sim$0.1 s) [51]. Due to the high repetition rate of the laser pulses present over a significant illumination time, the excited electrons can be pushed away by the optical rectification field from volume elements where the product of the light fields, $E^*(2\omega; \vec{r}) \cdot E(\omega; \vec{r})^2$, is large, towards trap sites in the direction given by the rectification field. If the optical rectification field is not strong enough, recombination will be dominant and no charge grating is written, *i.e.*, the average IR laser power should be above a threshold, which is in agreement with our experimental observation (*cf.* Fig. 3(e)).

To illustrate the shape of charge distribution written in the core of the waveguide, we have calculated the product $E(\omega; \vec{r})^2 E^*(2\omega; \vec{r}) \propto \mathcal{E}$ and used Poisson's equation, simplified to $\rho(x) \propto d\mathcal{E}/dx$, where ρ is the charge density, to determine from the transverse field the according charge density. Figure 8 shows the example of a charge distribution as generated by the pump radiation in the E_{11} mode and by SH in the E_{13} mode, both having a horizontal polarization. For better clarity of presentation, only charge levels with $|\rho|$ in the range of 80% - 100% of the maximum charge are shown. Positive and negative charge are indicated by red and blue, respectively. Figure 8 shows that the overlapping pump and SH fields generate a charge grating where the longitudinal periodicity defines a grating period, $\Lambda = 2\ell_c = \frac{2\pi}{\Delta k}$, where ℓ_c is the coherence length for second-harmonic generation in absence of quasi-phase matching. This grating period is what is required for quasi-phase matched (QPM) generation of the second harmonic field.

At this point it can be discussed, why not all of the allowed spatial modes are equally likely to generate a SH output. We suggest that the answer lies in the very different charge patterns that correspond to the different pump and SH mode combinations. As can be seen in Fig. 8 the longitudinal grating period, Λ, is set by the wavenumber mismatch between the mode of the IR pump, here taken to be the fundamental E_{11} mode, and the mode of the SH field. A smaller phase mismatch, Δk, and consequently a larger grating period, Λ, results in a stronger growth
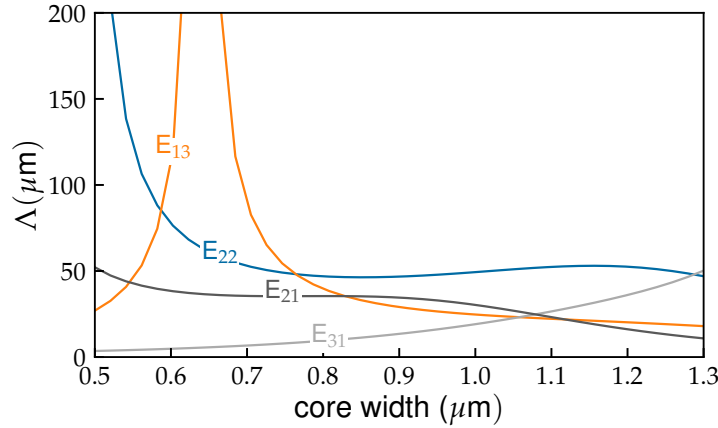
Fig. 9. QPM period required for SHG in the various different modes shown in Fig. 1 with the infrared pump power in the E_{11} mode. All modes are horizontally polarized. As can be seen, E_{13} has the largest period for the range of waveguide widths discussed in Fig. 1.

with distance for the SH in the waveguide [47]. Initially, the SH field might be emitted in various modes. But then, during the initiation phase of exponential growth, the various resulting charge gratings will compete with each other to establish the charge grating in the waveguide. The mode with the largest growth, *i.e.*, with the smallest phase mismatch, will become the dominant mode due to the nonlinear feedback process described above. Figure 9 depicts the QPM period, Λ, as a function of the width of the waveguide core for various modes with horizontal polarization.

Figure 9 shows that, for a waveguide width of $w = 0.7$ μm *i.e.*, for the waveguide used to record the SH beam profile in Fig. 6(a), the required QPM period, Λ, is rather short for most of the SH modes, and consequently these modes will only experience a moderate growth. Only certain modes, here E_{13}, can be quasi-phase matched with a long QPM period and will experience a far larger growth, *i.e*, will become the dominant mode. This is in agreement with the measured SH beam profile (see Fig. 6(a)).

As a related conclusion, from Fig. 9, it appears more likely that the observed SH output is a E_{13}-E_{21} superposition (with dominating E_{13}) than having a E_{31} contribution. The E_{31} contribution, that may be present in the observed SH intensity distribution, requires an even shorter QPM period at $w = 0.7$ μm and is expected to have a smaller growth. Based on these phase-matching arguments, Fig. 9 would imply that SH generated in the E_{22} mode grows faster than that generated in the E_{21} mode. However, this mode is not expected to grow due to the zero on-axis intensity of the E_{22} mode, which creates a poor modal overlap of this mode with the E_{11} mode of the IR pump.

In order to quantify the nonlinear susceptibility than can be provided by the CPGE in Si_3N_4 waveguides, we proceeds as follows. We consider an equivalent waveguide of the same length having a homogeneous second order nonlinearity, and we calculate the equivalent second-order susceptibility, $\chi_{eq}^{(2)}$, required to produce the same SH power as the Si_3N_4 waveguide assuming perfect phase matching and no pump depletion. For this case, the relation between the coefficient of nonlinear coupling, κ, and the equivalent second-order nonlinear susceptibility, $\chi_{eq}^{(2)}$, is given by [31]

$$\chi_{eq}^{(2)} = 2\sqrt{\left(\frac{\kappa}{\varepsilon_0}\right)^2 \frac{2(n(\omega)_{eff})^2 \, n(2\omega)_{eff}}{(2\omega)^2} \left(\frac{\mu_0}{\varepsilon_0}\right)^{-3/2} S_{eff}}. \tag{9}$$
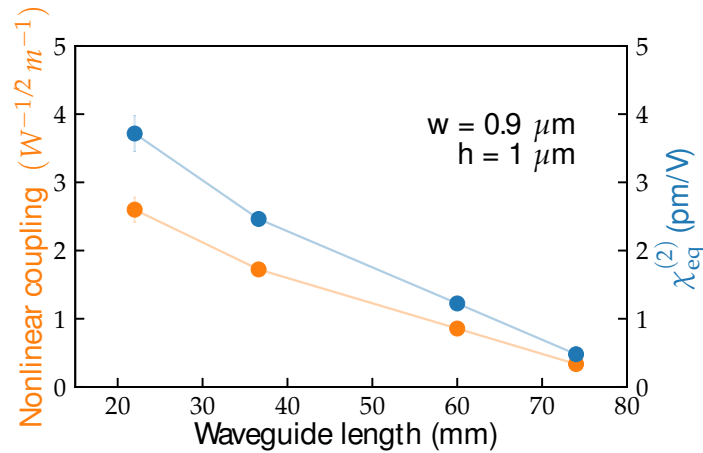
Fig. 10. Nonlinear coupling (orange markers) and equivalent $\chi^{(2)}_{\text{eq}}$ (blue markers) as a function of the length of the waveguide. The core of the waveguide has a cross-section of $0.9 \times 1 \ \mu\text{m}^2$. The shown error bar (0.2 pm/V half-width) seen at the highest data points represents the statistical uncertainty of the fit in Fig. 4 and the experimental uncertainty in measuring the output coupling efficiency at the waveguide exit facet.

Here, $n_{\text{eff}}(\omega)$ and $n_{\text{eff}}(2\omega)$ are the effective refractive indices for the IR and SH waves, while S_{eff} is the effective cross-section of the modal overlap of the IR and the SH fields [31], which are assumed to be the same for both the Si_3N_4 and equivalent waveguides. The coefficient of nonlinear coupling, κ, in Eq. (9) can be obtained from the measured conversion efficiency, η, via

$$\eta = P(2\omega)/P_0(\omega) = \kappa^2 P_0(\omega) L^2, \tag{10}$$

where $P(2\omega)$ and $P_0(\omega)$ are the generated SH power and the input IR power, respectively, and L is the length of the waveguide. In our case, the horizontally polarized pump radiation is injected in the E_{11} mode and the SH is dominantly generated in the E_{13} mode with the same polarization. Figure 10 shows the nonlinear coupling, κ, for the equivalent waveguide as a function of the length of the waveguide as calculated from the data in Fig. 7(b). Also shown is the corresponding equivalent second-order susceptibility as calculated using Eq. (9), assuming a pure E_{13}-mode for the SH output. Figure 10 shows that the maximum value for $\chi^{(2)}_{\text{eq}}$ obtained in this way is about 3.7±0.2 pm/V. We note that taking into account a small SH contribution in the E_{21} mode would lead to a larger equivalent susceptibility. Figure 10 shows that $\chi^{(2)}_{\text{eq}}$ decreases monotonically with increasing length of the waveguide. This is due to saturation of the SH output, as can be seen in Fig. 7(b), and our definition of $\chi^{(2)}_{\text{eq}}$.

4. Summary and conclusions

For the first time, we have observed second-harmonic generation in LPCVD-grown stoichiometric Si_3N_4 waveguides. Second-harmonic output was generated independent of the width of the waveguide core cross-section and required a build-up, a delay in the order of several minutes up to hours and an exponential growth to a steady state value, depending on the IR pump power and waveguide core cross-section. These findings are consistent with the coherent photogalvanic effect being responsible for the building up of a second-order nonlinearity and quasi-phase matching. With the available pump laser pulses, the investigated Si_3N_4 waveguides provide a maximum conversion efficiency of 0.4% for an input power of 13 mW (peak power 105 W,

pulse energy of 0.65 nJ). This is the highest second-order conversion efficiency achieved to our knowledge in an integrated SiN platform. The measured conversion efficiency corresponds to a high equivalent second-order susceptibility, $\chi_{eq}^{(2)} = 3.7\pm0.2$ pm/V. Although highly Si-rich SiN thin films might be expected to yield a somewhat larger value as concluded from photoelectron spectroscopy ($\chi_{eff}^{(2)} = 11.8$ pm/V [25]), the second order susceptibility that we find is larger than in SiN thin films ($\chi_{eff}^{(2)} = 2.5$ pm/V [24]), is one order of magnitude larger than in stress-released Si_3N_4 waveguides ($\chi_{eff}^{(2)} = 0.3$ pm/V [27]) and more than two orders of magnitude larger than in Si_3N_4 ring resonators ($\chi_{eff}^{(2)} < 0.04$ pm/V) [26].

Numerous applications are already based on $\chi^{(1)}$-gratings in waveguides such as reconfigurable Bragg filters [6], optical switching [31, 52], mode conversion [53] or optical storage [10]. The presence of an effective $\chi^{(2)}$-grating in amorphous Si_3N_4 waveguides may lead to the development of further functionalities such as parametric down-conversion [54], all optical signal processing [52], and possibly also self-referencing of frequency combs that exploits the simultaneous presence of $\chi^{(2)}$ and $\chi^{(3)}$ in low-loss Si_3N_4 waveguides [55–57].